Elimination of Saturation Effects in Sensorless Position Controlled Induction Motors

Joachim Holtz, *Fellow, IEEE*, and Hangwen Pan
Electrical Machines and Drives Group, University of Wuppertal
42097 Wuppertal – Germany

Abstract – **Owing to the variable magnetic coupling between the stator windings and the discrete rotor bars of an induction motor, a quasi-continuous rotor position signal can be acquired by instantaneous measurement of the total leakage inductance of the three stator phases. The signals are sampled in synchronism with the regular commutations of the PWM process, thus making the injection of additional high-frequency carriers obsolete. The acquired position signal exhibits high spatial resolution and high dynamic bandwidth.**

Magnetic saturation also influences upon the total leakage inductances and hence constitutes a disturbance for position identification. The paper presents a detailed analysis of the saturation effects and proposes methods to eliminate their undesired impact on the position signal. Experimental results of closed loop sensorless position control at full load and high dynamic performance are presented.

Keywords: Sensorless control, position control, zero speed control, magnetic saturation

I. INTRODUCTION

Sensorless position control of induction motors is a newly emerging technology. It exploits magnetic or electric anisotropies of the rotor that are inherently existing or, alternatively, intentionally introduced. Among the various phenomena, one class of anisotropies is characterized by having its spatial orientation in a fixed relation to the angular position of the rotor. Another class of anisotropies is induced by magnetic saturation. These anisotropies are tied to the spatial orientation of the angular position of the revolving fundamental field.

The directions in space of such anisotropies are generally identified from the response of the machine to perpetuate transient excitation through the stator windings. Signal processing methods then serve to identify the actual rotor position angle, or the fundamental field angle.

For the estimation of the rotor position angle, two different methods have been investigated in the past:

- the frequency domain approach, *Lorenz et al* [1, 2, 3], *Asher et al* [4, 5, 6]
- the time domain approach, *Jiang* [7], *Pan* [8], *Holtz* [9]

Both methods rely on anisotropy effects that induction motors exhibit if subjected to transient excitation. The frequency domain approach establishes a transient condition by continuously injecting a high-frequency carrier signal into the stator windings. The position information is reflected in the negative sequence component of the response signal. It is extracted by phase locked loop techniques. Adverse effects are the dead time phenomena of the inverter, the parameter dependency,

the low signal-to-noise ratio, the dynamic delay of the phase locked loop, and magnetic saturation caused by the fundamental field. It is particularly the saturation effects that have so far impeded the application of this estimation technique in fully loaded closed loop position control systems [3, 5].

The second method operates in the time domain. Here, instantaneous samples are taken of the stator phase voltages, immediately after the inverter commutations that occur at PWM operation. The switching of the inverter provides much higher transient excitation than the injection of a continuous carrier, thus contributing to a high signal to noise ratio. The sampled stator phase voltages serve to compute the zero sequence voltage component. This quantity reflects, among other effects, an existing unbalance at the sampling instant between the total leakage inductances of the three phases. Such unbalance has different origins:

1. The variation of magnetic coupling between the stator windings and the rotor bars. The degree of magnetic coupling depends on the relative position of the rotor bars with respect to the stator phase windings;

2. the local saturation of the leakage flux paths in the neighborhood of the maximum of the magnetic flux density distribution of the fundamental field, and

3. the modulation of the local leakage flux density by intentionally engineered modifications of the geometric dimensions of the rotor slots or the rotor bars.

If the first effect is utilized to extract the desired position signal, the magnetic saturation of the second effect acts as a disturbance. Its elimination is the subject of this paper. As only standard induction machines with open rotor slots are considered here, the third effect does not exist.

II. MACHINE ANISOTROPIES

A. Transient leakage fields

The anisotropies of an induction motor that produce the aforementioned effects are detected by subjecting the machine to transient excitations. The regular PWM waveforms of the phase voltages already exhibit the required fast excursions from their fundamental components. While the fundamental components of the stator voltages generate a flux density distribution that links with the winding conductors both in the stator and in the rotor, the transient flux components, owing to their high-frequency content, do not penetrate sufficiently fast through rotor surface to establish mutual flux linkages. These fluxes, instead, create only separate linkages with the respective stator and rotor windings, thus contributing to the
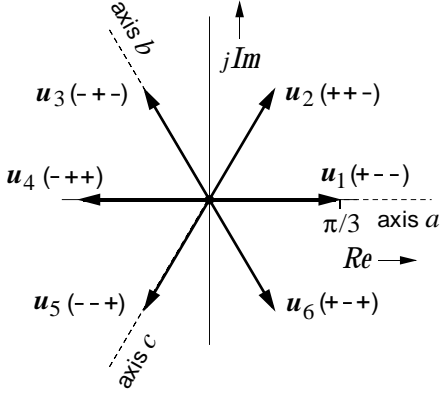
Fig. 1. Locations of the active switching state vectors u_k, $k = 1 \ldots 6$

total leakage flux.

The detailed study in [10] shows that the fundamental flux density wave in any given operating point and the transient leakage fields that result from an additional step-like excitation can be separately analyzed. The total flux linkage distribution is subsequently obtained as the superposition of the fundamental and the transient component.

In accordance with these results, the following analysis refers only to the transient leakage fields. These are represented by the space vector of the transient leakage flux linkages

$$\boldsymbol{\psi}_{\sigma\mathrm{tr}} = \boldsymbol{l}_\sigma \boldsymbol{i}_\mathrm{tr} \tag{1}$$

where $\boldsymbol{i}_\mathrm{tr}$ is the current component produced by a voltage transient $\boldsymbol{u}_\mathrm{tr}$, and $\boldsymbol{l}_\sigma$ is tensor of the total leakage inductance as will be presently explained. In the event of an inverter commutation, the transient stator voltage component

$$\boldsymbol{u}_\mathrm{tr} = \boldsymbol{u}_\mathrm{s} - \boldsymbol{u}_\mathrm{s1} \tag{2}$$

produces a change of the leakage flux vector

$$\frac{d\boldsymbol{\psi}_{\sigma\,\mathrm{tr}}}{d\tau} = \boldsymbol{l}_\sigma \frac{d\boldsymbol{i}_\mathrm{tr}}{d\tau} + \boldsymbol{i}_\mathrm{tr} \frac{d\boldsymbol{l}_\sigma}{d\tau} = \boldsymbol{u}_\mathrm{tr} \tag{3}$$

which adds to the fundamental component $\boldsymbol{\psi}_{\sigma1}$. In (2), $\boldsymbol{u}_\mathrm{s1}$ is the fundamental stator voltage associated to an assumed steady-state condition that prevails before the commutation. All space vector variables are normalized using the rated peak stator voltage $\sqrt{2}\boldsymbol{u}_\mathrm{sR}$, the rated peak stator current $\sqrt{2}\boldsymbol{i}_\mathrm{sR}$, and the nominal stator frequency ω_sR as base quantities. Note that time is also normalized, $\tau = \omega_\mathrm{sR}t$.

B. The leakage inductance tensor

The conventional model of the induction motor assumes the leakage inductances of the three phases as balanced. This balance is disturbed in the presence of machine anisotropies, giving rise to different leakage inductance values in the respective phases. The space vector $\boldsymbol{u}_\mathrm{tr}$ of the transient voltage component then produces an excursion of the vector $\boldsymbol{i}_\mathrm{tr}$ in a spatial direction that differs from that of the vector $\boldsymbol{u}_\mathrm{tr}$. This requires representing the leakage inductance in (1) and (3) by the tensor $\boldsymbol{l}_\sigma$ instead of the customary scalar coefficient l_σ.

To elaborate on this, reference is made to the switching state vectors of a two-level inverter, the locations of which are shown in Fig. 1. The vectors are normalized in amplitude using the peak value of the fundamental stator voltage at six-step operation $\hat{u}_{1\,\mathrm{six\text{-}step}} = \sqrt{2}\cdot\sqrt{2}/\pi\cdot U_\mathrm{d}$ as the base quantity, from which $|\boldsymbol{u}_\mathrm{k}| = \pi/3$, $k = 1 \ldots 6$, follows. When the vector $\boldsymbol{u}_1$ is turned on, a transient excitation by $\boldsymbol{u}_\mathrm{tr} = \pi/3$ occurs in
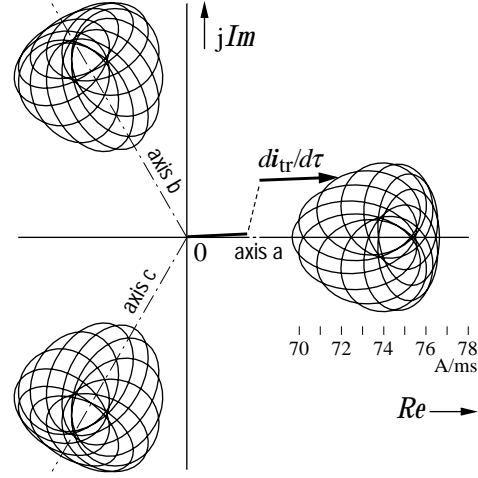
Fig. 2. Loci of the vector $di_\mathrm{tr}(\vartheta, \delta)/dt$ at transient excitation in the directions of the three phase axes (Note the suppressed origin)

the direction of the a-axis. Owing to the machine anisotropies, the resulting current component $\boldsymbol{i}_\mathrm{tr}$ builds up in a different direction. The deviation of its derivative $di_\mathrm{tr}/d\tau$ from the direction of $\boldsymbol{u}_\mathrm{tr}$ is governed by the leakage inductance tensor in (3).

The following anisotropies inherently exist in an induction machine:

- the anisotropy of the squirrel cage rotor, having a spatial orientation that rotates in synchronism with the rotor position angle ϑ, and
- the anisotropy induced by magnetic saturation through the fundamental field, which rotates in synchronism with the field angle δ.

Under these influences, the derivative vector $di_\mathrm{tr}(\vartheta, \delta)/d\tau|_\mathrm{a}$ – immediately after the commutation to $\boldsymbol{u}_1$ is completed – locates on one point of the epicyclic curve centered on the real axis in Fig. 2. The spatial high-frequency component of this curve is caused by the rotor anisotropy, while the low-frequency component is owed to magnetic saturation.

A different derivative vector $di_\mathrm{tr}(\vartheta, \delta)/d\tau|_\mathrm{b}$ is produced by a transient excitation in the direction of the b-axis through the switching state vector $\boldsymbol{u}_3$. This vector points to a location on the epicyclic pattern centered on the b-axis as shown in Fig. 2. Finally, an excitation in the direction of the c-axis through $\boldsymbol{u}_5$ gives rise to a vector $di_\mathrm{tr}(\vartheta, \delta)/d\tau|_\mathrm{c}$ which targets the pattern centered on the c-axis.

The following conditions are introduced to simplify the mathematical analysis of the anisotropies:

- Given the properties of a two-level inverter, transient excitations occur only in the directions of the three phase axes.
- Of the product $\boldsymbol{l}_\sigma di_\mathrm{tr}(\vartheta, \delta)/d\tau$ in (3), only the components in the direction of the phase axes will be computed. The characteristic quantities are then scalar inductance components $l_{\sigma\mathrm{a}}$, $l_{\sigma\mathrm{b}}$, and $l_{\sigma\mathrm{c}}$ of the respective phase axes.
- Accurate position estimation is only required at very low speed. Changes with time of the inductance tensor are then small which permits neglecting the term $\boldsymbol{i}_\mathrm{tr}d\boldsymbol{l}_\sigma/d\tau$ in (3).
- It is assumed that the laminations of the rotor iron are sufficiently thin such that the eddy currents generated by the switching of the inverter are small in comparison with the induced currents in the rotor bars.
- Rotor eccentricity is not considered.

C. Leakage inductance model

The anisotropic characteristics of an induction machine result from a combination of three different effects that will be analyzed in the following.

C.1 Rotor anisotropy

As an introduction to this phenomenon, consider an unsaturated 2-pole induction motor having only two rotor bars. These are spaced over the full pole pitch and short-circuited through the end rings, thus forming a single rotor winding. It is obvious from Fig. 3 that the mutual inductance between the rotor winding and the phase winding a is

Fig. 3. A primitive induction machine having only two rotor bars

zero at $\vartheta = \pi/2$ and $\vartheta = 3\pi/2$, and maximum at $\vartheta = 0$ and $\vartheta = \pi$. Assuming a sinusoidal flux density distribution in the airgap, the mutual inductance

$$l_m(\vartheta) = l_m(0) \cos \vartheta. \qquad (4)$$

The total leakage inductance of phase winding a

$$l_{\sigma a}(\vartheta) = l_s \left(1 - \frac{l_m^2(\vartheta)}{l_s l_r} \right) \qquad (5)$$

depends on the square of l_m which makes it positive throughout. In (5), l_s is the stator inductance and l_r is the rotor inductance.

A squirrel cage rotor of a real machine may have $n_{rp} = n_r/p$ rotor bars per pole pair, where n_r is the number of rotor bars and p is the number of pole pairs. Also here does the mutual inductance vary with the rotor position. The total leakage inductance of phase a is a periodic function of the rotor position angle ϑ, [7]. A full cycle of this function completes when the rotor displaces by one rotor slot pitch.

For the three stator phases, the dependence on the rotor slot effect of the total leakage inductances are described in good approximation by their fundamental components

$$l_{\sigma\,slot}(\vartheta) = l_{\sigma 0} \left(1 + \frac{l_{\sigma\,slot\,0}}{l_{\sigma 0}} cos \left(n_{rp} \left(\vartheta - (k-1) \frac{2\pi}{3} \right) \right) \right) \qquad (6)$$

where $l_{\sigma 0}$ is the average leakage inductance value, $l_{\sigma\,slot\,0}$ is the amplitude of the leakage inductance variations, and $k = 1, 2, 3$ refers to the phases a, b, and c, respectively.

A rotor anisotropy exists when the phase values of the total leakage inductances differ from each other. This is always true when the number n_{rp} of rotor bars per pole pair is not a multiple of three. It is easily seen that three – or an entire multiple of three – rotor bars in an arrangement similar to that of Fig. 3 would lead to balanced leakage inductances in

the three stator phases. Although their values vary with the rotor position angle, they do not constitute an anisotropy. Squirrel cage rotors having $3k\,n_{rp}$ rotor bars, however, are rarely used since they produce higher torque ripple.

C.2 Saturation through the magnetizing field

The magnetizing component of the fundamental flux density distribution saturates the iron of the stator and rotor teeth in the neighborhood of the spatial maximum of the flux density wave. The saturation changes the permeance of the leakage flux paths in the stator and the rotor and thus affects the total leakage inductances. Assuming a massive rotor without rotor bars, the effect is approximated by the fundamental components of the total leakage inductances per phase

$$l_{\sigma\,sat}(\delta) = l_{\sigma 0} \left(1 + \frac{l_{\sigma\,sat\,0}}{l_{\sigma 0}} cos\,2 \left(\delta - (k-1) \frac{2\pi}{3} + \varphi_{sat} \right) \right) \qquad (7)$$

where $l_{\sigma 0}$ is the average leakage inductance value and $l_{\sigma\,sat\,0}$ is the amplitude of the leakage inductance variations. The angle $\varphi_{sat} = 0$ if the angular displacement of the magnetizing field counts from stator phase a, as is customary.

The effect of magnetic saturation on the anisotropies of a squirrel cage machine is twofold:

- Saturation changes the permeance of the leakage paths as a function of the magnetizing flux density distribution, and of the field angle δ. The effect is represented by (7).
- The changing permeance of the leakage paths also affects the amplitude $l_{\sigma\,slot\,0}$ in (6) of the rotor slot dependent variation of the total leakage inductance.

The combined effect is described by taking the product of (6) and (7), and by introducing in (6) a saturation dependent amplitude modulation factor

$$\left(1 + k_m \frac{l_{\sigma\,sat\,0}}{l_{\sigma\,slot\,0}} cos\,2 \left(\delta - (k-1) \frac{2\pi}{3} \right) \right) \qquad (8)$$

which models the saturation influence due to a sinusoidal distribution of the fundamental field. $k_m = 0.2 \ldots 0.5$ in (8) is a constant, machine dependent coefficient. The resulting total leakage inductances of the three phases are functions of the rotor position angle ϑ and the field angle δ:

$$l_\sigma(\vartheta, \delta) = l_{\sigma 0} \left(\begin{array}{c} \left(1 + \frac{l_{\sigma\,slot\,0}}{l_{\sigma 0}} \left(1 + k_m \frac{l_{\sigma\,sat\,0}}{l_{\sigma\,slot}} cos\,2 \left(\delta - (k-1) \frac{2\pi}{3} \right) \right) \right) \\ \cdot cos \left(n_{rp} \left(\vartheta - (k-1) \frac{2\pi}{3} \right) \right) \end{array} \right)$$
$$\cdot \left(1 + \frac{l_{\sigma\,sat\,0}}{l_{\sigma 0}} cos\,2 \left(\delta - (k-1) \frac{2\pi}{3} \right) \right) \qquad (9)$$

To illustrate the characteristics of (9), the effects of machine anisotropies on the total leakage inductance are illustrated in Fig. 4(a). This simulation assumes the induction motor running at no-load and 1 Hz stator frequency.

C.3 Saturation caused by the load current

The machine is additionally exposed to current components that magnetize the q-axis when a load torque is applied, thus
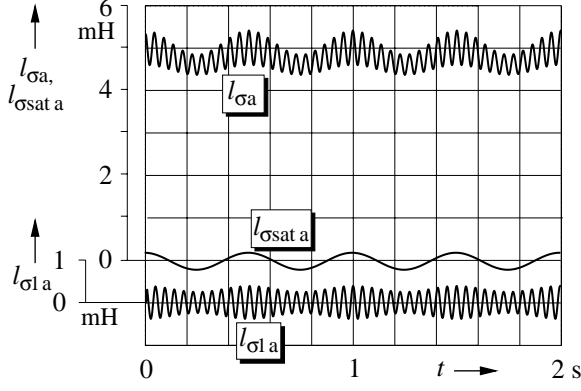
(a) Variations of the phase-*a* leakage inductance components. The curve $l_{\sigma l\,a}$ represents $l_{\sigma\,slot\,a}$ from (6), but amplitude modulated by the term (8)
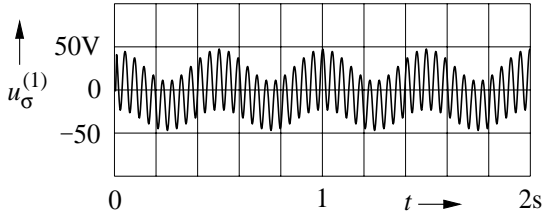
(b) The corresponding anisotropy signal

Fig. 4. Effect of machine anisotropies at no-load operation, 1 Hz stator frequency (Simulation)

changing the conditions of saturation. While a theoretical analysis of the phenomenon is not given here, Section IV.A addresses ways of its compensation.

III. SIGNAL ACQUISITION

It was demonstrated in the previous Section that the leakage inductances of the three stator phases are influenced by the machine anisotropies and their spatial orientations. These are characterized by the rotor position angle ϑ and the field angle δ. Measuring the individual values of the phase leakage inductances is therefore a clue to identifying either the position angle, or the field angle, or both.

One way of acquiring an anisotropy signal is measuring the transient zero sequence voltage of the stator winding, defined as the sum of the three phase voltages

$$u_\sigma = u_a + u_b + u_c \tag{10}$$

of a star connected stator winding. The notation u_σ relates to the transient leakage effect. Since the induced voltages u_{ia}, u_{ib} and u_{ic} do not exhibit a zero sequence component,

$$u_{ia} + u_{ib} + u_{ic} = 0, \tag{11}$$

the anisotropy signal from (10), (11) and Fig. 5 is

$$u_\sigma = l_{\sigma a}\frac{di_a}{d\tau} + l_{\sigma b}\frac{di_b}{d\tau} + l_{\sigma c}\frac{di_c}{d\tau}. \tag{12}$$

The transient excitation that generates such signal is produced by the switching of the PWM inverter. Assuming that the switching state vector $\boldsymbol{u}_1$ has been turned on (Fig. 1), the
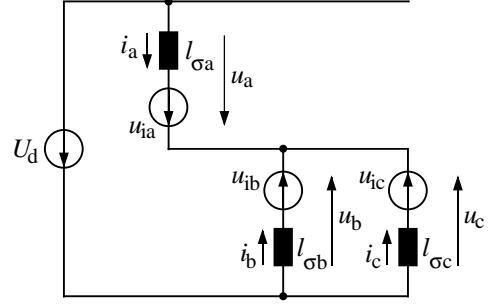

Fig. 5. Equivalent circuit of the induction motor with the switching state $\boldsymbol{u}_1$ applied

three stator phase potentials are $u_a{'} = u_d/2$ and $u_b{'} = u_c{'} = -u_d/2$, and u_σ in (12) is now named $u_\sigma^{(1)}$. This establishes the circuit topography of Fig. 5. The following equations hold

$$u_d = l_{\sigma a}\frac{di_a}{d\tau} + u_{ia} - l_{\sigma b}\frac{di_b}{d\tau} - u_{ib} \tag{13}$$

$$u_d = l_{\sigma a}\frac{di_a}{d\tau} + u_{ia} - l_{\sigma c}\frac{di_c}{d\tau} - u_{ic} \tag{14}$$

$$i_a + i_b + i_c = 0 \tag{15}$$

The anisotropy signal $u_\sigma^{(1)}$ that is generated by the switching state vector $\boldsymbol{u}_1$ is obtained by solving (10) through (15). The result is

$$u_\sigma^{(1)} = u_d\frac{l_{\sigma a}\left(l_{\sigma b} + l_{\sigma c}\right) - 2l_{\sigma b}l_{\sigma c}}{l_{\sigma a}l_{\sigma b} + l_{\sigma b}l_{\sigma c} + l_{\sigma a}l_{\sigma c}} + u_{\sigma i}, \tag{16}$$

where the term

$$u_{\sigma i} = 3\frac{l_{\sigma a}l_{\sigma b}u_{ic} + l_{\sigma a}l_{\sigma c}u_{ib} + l_{\sigma b}l_{\sigma c}u_{ia}}{l_{\sigma a}l_{\sigma b} + l_{\sigma b}l_{\sigma c} + l_{\sigma a}l_{\sigma c}} \tag{17}$$

summarizes the contribution of the induced voltages. These are small at low speed and hence can be neglected, as explained at the end of this Section.

The signal $u_\sigma^{(1)}$ reflects the changes of the total leakage inductances, primarily those of the phase-*a* component $l_{\sigma a}$, as demonstrated in Fig. 4. A close inspection of these curves reveals some remarkable differences between $l_{\sigma a}$ and $u_\sigma^{(1)}$:

• The amplitude of the rotor slot induced high-frequency oscillation is much more uniform in the signal $u_\sigma^{(1)}$.
• Other than the signal $l_{\sigma a}$, the acquired anisotropy signal $u_\sigma^{(1)}$ does not exhibit a dc offset.

The formal reason for these favorable differences is in the nonlinear mapping of the phase leakage inductances on the anisotropy signal (16). The summing of the phase voltages in (10) further eliminates all nonsignificant fundamental and large offset components. Therefore, the small changes in the curve $l_{\sigma a}$ transform to a balanced ac signal having a remarkable amplitude of more than 50 V. This establishes a very high signal-to-noise ratio.

When the switching state vector $\boldsymbol{u}_4 = -\boldsymbol{u}_1$ is applied to the machine, the stator phase potentials are $u_a{'} = -u_d/2$ and $u_b{'} = u_c{'} = u_d/2$. The anisotropy signal is then

$$u_\sigma^{(4)} = -u_\mathrm{d} \frac{l_{\sigma\mathrm{a}}\left(l_{\sigma\mathrm{b}} + l_{\sigma\mathrm{c}}\right) - 2l_{\sigma\mathrm{b}}l_{\sigma\mathrm{c}}}{l_{\sigma\mathrm{a}}l_{\sigma\mathrm{b}} + l_{\sigma\mathrm{b}}l_{\sigma\mathrm{c}} + l_{\sigma\mathrm{a}}l_{\sigma\mathrm{c}}} + u_{\sigma\mathrm{i}}, \qquad (18)$$

where the term $u_{\sigma\mathrm{i}}$ is again negligible. The anisotropy signals that associate to the switching state vectors u_2 and u_5, and to u_3 and u_6, are obtained by cyclically replacing the phase indices in (16) and (18), respectively.

While two adjacent switching state vectors, e.g. u_1 and u_2, form part of a regular modulation sequence, a third vector having a $2\pi/3$ phase displacement with each of the other two vectors, e.g. u_3, is introduced when needed by modifying the original pattern from $u_0 - u_1 - u_2$ to $u_0 - u_1 - u_2 - u_3 - u_6$, where very short vectors u_3 and u_6 are added to replace the zero vector.

The three acquired signals

$$\begin{aligned} u_{\sigma\mathrm{a}} &= u_\sigma^{(1)} = -u_\sigma^{(4)} \\ u_{\sigma\mathrm{b}} &= u_\sigma^{(2)} = -u_\sigma^{(5)} \\ u_{\sigma\mathrm{c}} &= u_\sigma^{(3)} = -u_\sigma^{(6)} \end{aligned} \qquad (19)$$

are shown in Fig. 6 over an extended period of time. The error term $u_{\sigma\mathrm{i}}$ caused by the induced voltages as per (17) forms part of these waveforms. Its amplitude at 6.8 Hz stator frequency is 2.8 V, or 5% of the acquired signal amplitude. This justifies neglecting the error.

It is obvious from an inspection of the curves in Fig. 6 that their low-frequency components form a balanced three-phase system. This system is in synchronism with the saturation induced anisotropy and can serve to identify the field angle. It is further observed that the high-frequency components form another balanced three-phase system which is in synchronism with the rotor anisotropy and hence with the rotor position angle. To extract this information, the two components of the anisotropy signal must be separated.

IV. COMPONENT SEPARATION OF THE ANISOTROPY SIGNAL

A. *Spatial filtering*

The identification of the saturation related machine characteristics is done in a self-commissioning process. The obtained data are stored in a nonvolatile memory such that the procedure need not be repeated when the drive is restarted, unless a different machine is used.

The approach exploits the fact that the dominant frequencies of the two anisotropy signals are asynchronous, which is owed to the slip of the induction motor. This enables the separation of the field angle component from the rotor position component. The spatial digital filter shown in Fig. 7 is used for this purpose. Its input signals are the complex vector

$$u_\sigma = \frac{2}{3}\left(u_{\sigma\mathrm{a}} + a\, u_{\sigma\mathrm{b}} + a^2 u_{\sigma\mathrm{c}}\right) = u_{\sigma\alpha} + ju_{\sigma\beta}, \qquad (20)$$

formed by the components (19) of the anisotropy signal, and the field angle δ. Both signals are represented by n discrete elements per revolution of the fundamental field. The discretized values are referred to as $u_{\sigma\mathrm{k}}$ and δ_k, where $k = 1 \ldots n$. The coefficient "a" in (20) is the unity vector rotator
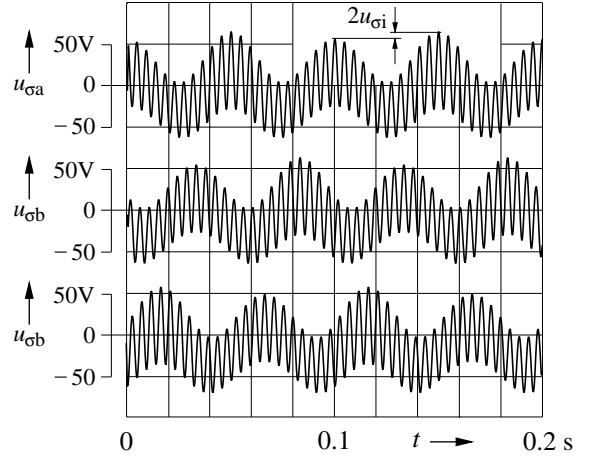

Fig. 6. Components of the anisotropy signal at no-load operation and 6.7 Hz stator frequency (Simulation)

$exp(\mathrm{j}2\pi/3)$.

The spatial filter extracts n discrete vector elements s_k that synthesize the vector $s(\delta_\mathrm{k})$ of the saturation component. A multiplexer MUX 1 assigns a value $u_{\sigma\mathrm{k}}$ to that filter channel k that the discretized field angle δ_k selects. Hence each filter channel processes only the signals the relate to a defined angular position of the fundamental field. The filters consist of memory cells s_k that store the value

$$s_\mathrm{k} = \alpha u_{\sigma\mathrm{k}} - (1-\alpha)s_\mathrm{k}' \qquad (21)$$

when δ_k is enabled, where s_k' is the memorized value that was stored when the field angle had rotated through the value δ_k on its previous revolution. The algorithm thus replaces s_k' by s_k whenever the fundamental field comes to align with the discrete position δ_k. It operates as a first-order filter having the filter time constant $\tau_\mathrm{f} = 1/\alpha$.

The n filters, each related to one particular value δ_k of the field angle, suppress the high-frequency components in u_σ that originate from the rotor anisotropy. To enable this, the machine must operate at nonzero slip to make the ratio of the two frequency components fractional, and the waveform pat-
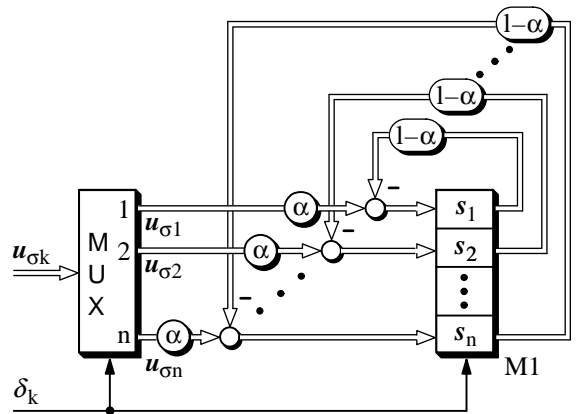

Fig. 7. Signal flow diagram of the spatial digital filter; the discretized saturation vectors s_k are stored in the memory M1, MUX is a multiplexer
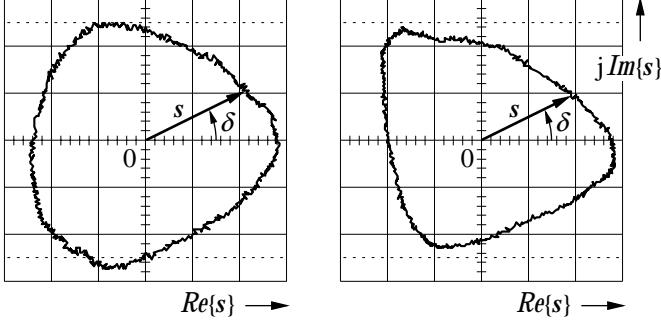
Fig. 8. Trajectories of the saturation vector $s(\delta, i_q)$ at no-load (left) and at 120% nominal load (right)

tern in Fig. 6 nonrepetitive. In practice, even the very small no-load slip serves the purpose.

Load current dependent saturation is identified by doing the spatial filtering at full load, and, if nonlinear conditions prevail, in one or two operating points of partial load. The acquired data sets $s(\delta, i_q)$ are individually stored. The recorded trajectories Fig. 8 of the saturation vector $s(\delta)$ show that its second harmonic component becomes conspicuous when the load increases to 120% nominal.

During regular operation, the data set that best matches the actual i_q-amplitude is selected for saturation compensation. If the saturation by the load current component is more pronounced with a particular machine, one would better interpolate between the data of two neighbored sets.

B. Analysis of the position signal

The contents of memory M1 in Fig. 7 is used to reconstruct the saturation vector $s(\delta)$, which represents the saturation induced component in $u_{\sigma k}$. Fig. 9 shows that the vector $s(\delta)$ is substracted from u_σ to obtain a position vector $p_r = p_r exp(j\vartheta_r)$, not considering the structure in the lower portion of Fig. 9 in a first step. The vector $p_r(\vartheta_r)$ rotates in synchronism with the high-frequency components in $u_{\sigma k}$ and hence, with its argument ϑ_r, indicates the angular displacement of the rotor within one rotor bar pitch. The magnitude of p_r bears no significance.

The derivative $d\vartheta_r/d\tau$ is the estimated speed $\hat{\omega}$. This signal is recorded in Fig. 10a, where the lower trace is the α-component of the position vector p'_r. The speed signal exhibits an apparently systematic distortion, the cause of which requires further investigation.

To this aim, the a-component of the total leakage inductance (9) is written as

$$l_{\sigma a} = l_{\sigma 0} + l_{\sigma \text{sat}0} \, cos(2\delta) + l_{\sigma \text{slot}0} \, cos(n_{\text{rp}}\vartheta)$$
$$+ k_2 l_{\sigma \text{sat}0} \, cos(2\delta) cos(n_{\text{rp}}\vartheta) \qquad (22)$$

where terms that comprise the product of two leakage inductances are neglected as being small, and k_2 is given in (24). Equations similar to (22) can be established for $l_{\sigma b}$, and $l_{\sigma c}$. These and (22) are inserted in (16). Again neglecting small product terms like $l_{\sigma \text{slot a}} \cdot l_{\sigma \text{slot b}}$, the component of an anisotropy signal that relates to a transient excitation by the switching state vector u_1 is obtained:
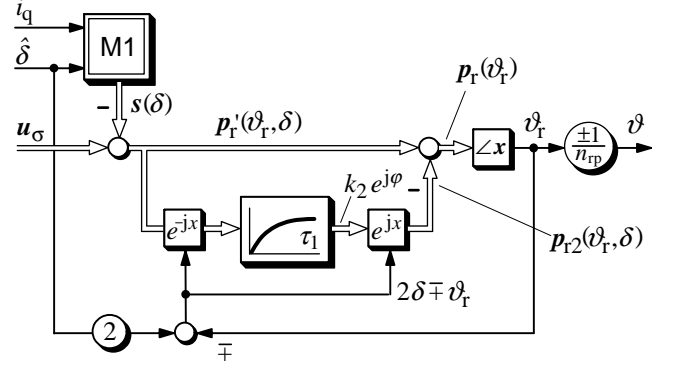

Fig. 9. Signal flow graph showing the generation of the rotor position angle ϑ from the anisotropy signal u_σ. The choice at the $\mp$-sign depends on the number of rotor bars.

$$u_\sigma^{(1)} = k_1 \left[l_{\sigma \text{slot}0} \, cos(n_{\text{rp}}\vartheta) + \frac{l_{\sigma \text{sat}0}}{2} k_2 \, cos(2\delta \mp n_{\text{rp}}\vartheta + \varphi_2) \right] \quad (23)$$

where $\qquad\qquad\qquad\qquad\qquad\qquad\qquad\qquad (24)$

$$k_1 = \frac{3 l_{\sigma 0} u_d}{l_{\sigma \text{abc}}^2}, \ k_2 = \frac{l_{\sigma \text{slot}}}{l_{\sigma 0}} + k_m, \ l_{\sigma \text{abc}}^2 = l_{\sigma a} l_{\sigma b} + l_{\sigma b} l_{\sigma c} + l_{\sigma a} l_{\sigma c}$$

The $\mp$-sign in (23) specifies whether the position vector rotates in the same, or in the opposite direction of the machine rotor, which depends on the number $n_{\text{rp}} = 3k \pm 1$ of rotor bars per pole.

Note that $u_\sigma^{(1)} = u_{\sigma a}$ according to (19). Assuming excitations by switching state vectors of other phase axes permits calculating the components $u_{\sigma b}$ and $u_{\sigma b}$ in a similar way. The three components are inserted in (20), from which the position vector

$$p'_r(\vartheta_r, \delta) = k_1 e^{j n_{\text{rp}} \vartheta} + k_2 e^{j(2\delta \mp n_{\text{rp}} \vartheta + \varphi_2)} \qquad (25)$$

(a) estimated speed obtained from p'_r
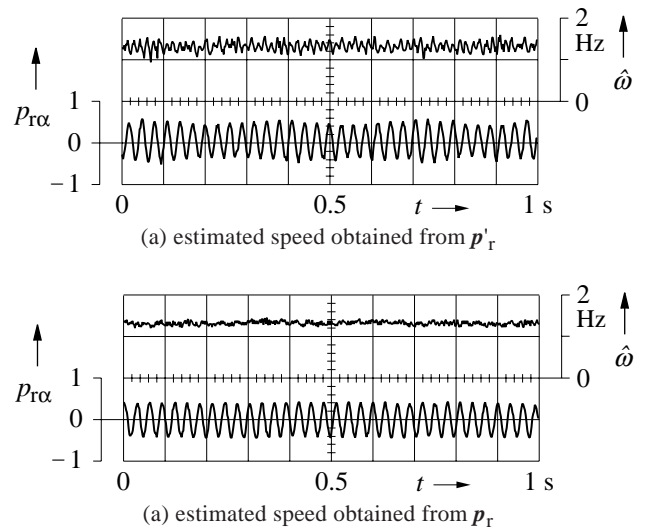

(a) estimated speed obtained from p_r

Fig. 10. α-component of the normalized position signal and estimated speed. The signals are normalized as represented in the software.
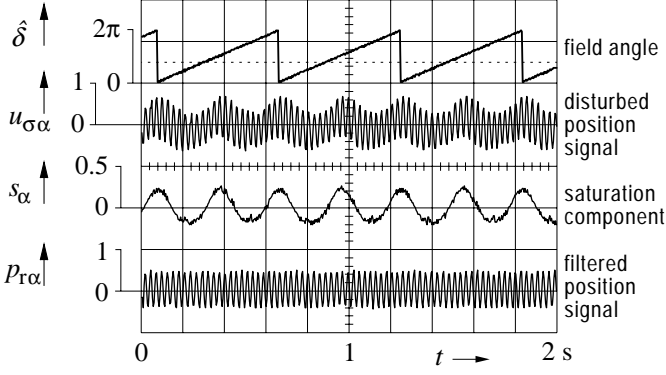
Fig. 11. Measured waveforms illustrating the elimination of saturation induced distortions from the position signal

Fig. 13: High-accuracy speed control at crawling speed; reversal from -0.2 % to $+0.2$ % of rated speed (± 0.1 Hz stator frequency)

is obtained. It is now apparent that an asynchronously rotating vector of amplitude k_2 adds to the true position vector, which is the cause of the oscillations in the speed signal Fig. 10(a). To eliminate this distortion, $\boldsymbol{p}'_r$ is transformed to a ($2\delta \mp n_{rp}\vartheta$)-reference frame, where the distortion vector, now having the constant value $k_2 \cdot exp(j\varphi_2)$, is separated by a low pass filter. Fig. 9 shows that the distortion vector is then retransformed to stationary coordinates and substracted from $\boldsymbol{p}'_r$ to yield an undistorted position vector $\boldsymbol{p}_r(\vartheta_r)$. The measured waveforms in Fig. 11 display the signals of this process. The resulting speed signal is shown in Fig. 10(b).

The argument of $\boldsymbol{p}_r(\vartheta_r)$, divided by the number n_{rp} of rotor bars per pole, yields the physical angular position ϑ of the machine rotor.

In a practical implementation, the rotor position ϑ within a full revolution is obtained by incrementing (or decrementing at reversed rotation) a modulo-n_{rp} counter whenever a full revolution of $\boldsymbol{p}_r$ is completed. Hence the incremental rotor position within a full revolution is

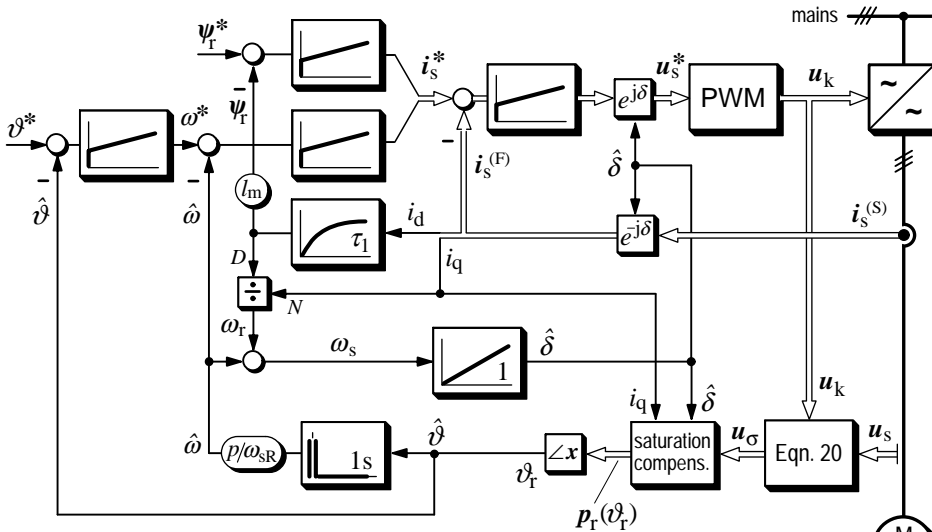$$\vartheta = (2\pi C_\vartheta + \vartheta_r)/pn_{rp} \qquad (26)$$

where C_ϑ is the state of the counter. The equation illustrates the nature of this sensorless position measurement, which is absolute and of high resolution within one slot pitch, and incremental in that the entire number of displaced rotor bars are counted. The quasi-instantaneous sampling of the anisotropy signal at 1 kHz or higher provides a high-bandwidth position signal, from which a speed signal is derived by differentiation.

V. EXPERIMENTAL RESULTS

The control system was implemented in a Siemens 80167 microcontroller of an industrial PWM inverter. The phase voltages were measured at the inverter output terminals and, for potential separation, transmitted to ground level as a high-frequency PWM modulated signal through small ferrite core transformers. Position acquisition at speed values above 10% nominal was done using rotor slot induced harmonic voltages [11]. A star-connected 4.5-kW induction motor was used, having $2p = 4$ poles and $N = 56$ rotor slots. The magnetic data are $l_{\sigma 0} = 4.78$ mH, $l_{\sigma\,slot\,0}/l_{\sigma 0} = 6.6\%$, $l_{\sigma\,sat\,0}/l_{\sigma 0} = 4.1\%$, $n_{rp} = 22$, and $k_m = 0.35$.

The signal flow diagram of the control system is shown in Fig. 12. Superimposed to a rotor field oriented current control system are separate controllers for the rotor flux linkage $\boldsymbol{\psi}_r$, and for speed and rotor position. The field angle δ is estimated using the rotor model of the machine. The drive system was operated at speed control and position control for the experimental evaluation.

Fig. 13 shows the performance at speed control during speed reversal between ± 10 rpm, or $6.7 \cdot 10^{-3}$ rated speed. In this situation, the motor takes 20 seconds to perform a full revolution of the its shaft.

Fig. 14 shows the character-

Fig. 12. Signal flow diagram of the drive control system
(S) and (F) refer to stator and field coordinates, respectively;
$\boldsymbol{u}_k$, $k = 1 \ldots 6$, are the switching state vectors; N: Numerator, D: Denominator
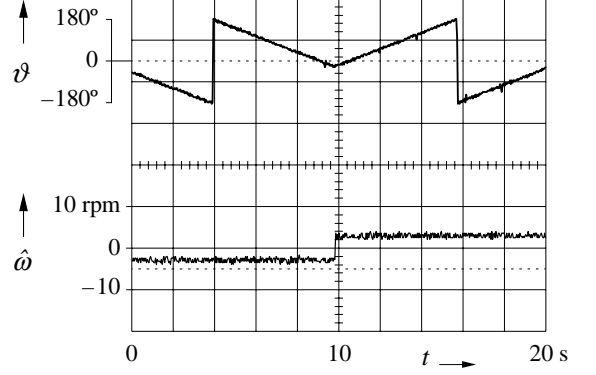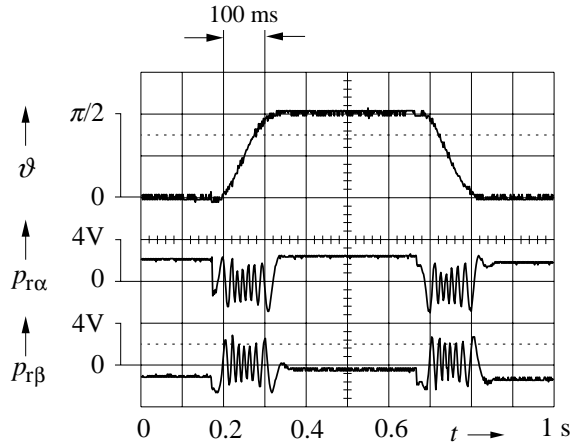
Fig. 14. Sensorless position control showing motor shaft displacement of ±90° at 120% rated transient torque; traces from top: shaft position angle ϑ, position signals $p_{r\alpha}$ and $p_{r\beta}$: constant values indicate zero speed.
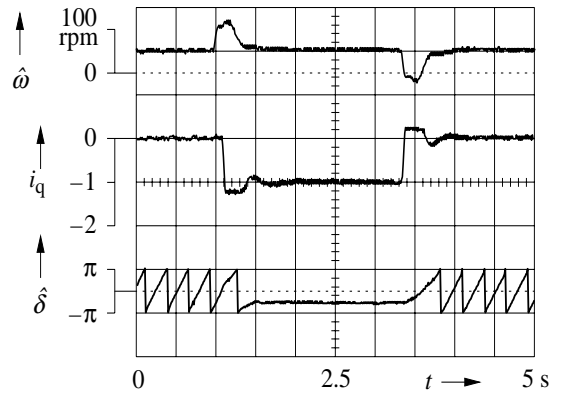

Fig. 15. Persistent operation at zero stator frequency with 120% rated torque applied. The steady-state process is initiated and terminated by transient commands; traces from top: estimated speed $\hat{\omega}$, normalized torque-building current i_q, field angle $\hat{\delta}$.

istic signals at closed-loop sensorless position control. A positioning cycle executing periodic variations of the motor shaft angle of ±90° produces transient torque excursions of 120% nominal value. It can be observed that the amplitudes of the position signals reduce temporarily during acceleration and deceleration. This is owed to magnetic saturation of the leakage paths; however, it has no detrimental effect on the accuracy of the position measurement.

Sustained operation at zero stator frequency, combined with high dynamic performance at 120% torque overload is demonstrated in Fig. 15. In this experiment, the machine is operated at speed control with the speed reference set to 50 rpm. This value corresponds to the slip speed at 120% torque overload. While operating initially without load, the system is subsequently subjected to a step change of 120% torque in the direction of rotation. Such disturbance causes a transient increase in speed which is compensated by a steeply rising negative torque current i_q. The motor regains its set speed immediately after the transient. The control masters the subsequent steady-state at zero stator frequency and 120% overload. Note that the field angle δ in the lower curve does not change. Even at zero stator frequency does the system maintain its full dynamic ability. The torque current i_q reacts instantaneously to the sudden removal of the external torque, reestablishing the set speed after a short transient speed drop.

VI. SUMMARY

The switched waveforms generated by a pulsewidth modulator subject an induction motor to perpetuate transient excitation. This permits identifying the spatial orientations of the inherent machine anisotropies. These relate to the rotor bar effect and to magnetic saturation. The former anisotropy rotates in synchronism with the rotor, the latter in synchronism with the magnetic field. A spatial filter is used for their separation. A high-bandwidth, high-resolution position signal is extracted at large signal-to-noise level. It enables accurate and high dynamic position control without sensor, and precise speed control at zero stator frequency.

VII. REFERENCES

1. P. L. Jansen and R. D. Lorenz, „Transducerless Position and Velocity Estimation in Induction and Salient AC Machines", *IEEE Trans. Industry Appl.*, Vol. 31, No. 2, Mar/Apr 1995, pp. 240-247.
2. M. W. Degner, R. D. Lorenz, „Using Multiple Saliencies for the Estimation of Flux, Position and Velocity in AC Machines", *IEEE Trans. Industry Appl.*, Vol. 34, No. 5, Sept/Oct 1998, pp. 11972-1104.
3. B. H. Kenny and R. D. Lorenz, „Stator and Rotor Flux Based Deadbeat Direct Torque Control of Induction Machines", *IEEE IAS Annual Meeting*, Chicago, 2001.
4. J. Cilia, G. M. Asher and K. J. Bradley, „Sensorless Position Detection for Vector Controlled Induction Motor Drives Using an Asymmetric Outer-Section Cage", *IEEE Trans. Industry Appl.*, Vol. 33, No. 5, Sept/Oct 1997, pp. 1162-1169.
5. N. Teske, G. M. Asher, M. Summer, and K. J. Bradley, „Suppression of Saturation Saliency Effects for the Sensorless Position Control Induction Motor Drives under Loaded Conditions", *IEEE Trans. Industry Appl.*, Vol. 47, No. 5, Oct 2000, pp. 1142-1149.
6. N. Teske, G. M. Asher, K. J. Bradley, and M. Summer, „Analysis and Suppression of Inverter Clamping Saliency in Sensorless Position Controlled Induction Motor Drives", *IEEE IAS Annual Meeting*, Chicago, 2001.
7. J. Jiang, „Sensorless Field Oriented Control of Induction Motors at Zero Stator Frequency" (in German), *Ph.-D. Dissertation*, Wuppertal University, 1999.
8. H. Pan, „Identification of the Rotor Position and the Field Angle by Indirect Measurement of the Leakage Inductance for Sensorless Control of Induction Motors at Zero Stator Frequency" (in German), *Ph.-D. Dissertation*, Wuppertal University, 2001.
9. J. Holtz, „Sensorless Position Control of Induction Motors – an Emerging Technology", *IEEE Trans. Ind. Electronics*, Vol. 45, No. 6, 1998, pp. 840-852.
10. J. Holtz, „On the Spatial Propagation of Transient Magnetic Fields in AC Machines", *IEEE Trans. Industry Appl.*, Vol. 32, No. 4, July/Aug. 1996, pp. 927-937.
11. J. Jiang, J. Holtz, „High Dynamic Speed Sensorless AC Drive with On-Line Parameter Tuning and Steady-State Accuracy", *IEEE Transactions on Industrial Electronics*, Vol. 44, No. 2, 1997, pp. 240-246.